JOURNAL OF PROPULSION AND POWER
Vol. 26, No. 6, November–December 2010

Leading-Edge Endwall Suction and Midspan Blowing to Reduce Turbomachinery Losses

Matthew J. Bloxham* and Jeffrey P. Bons†
Ohio State University, Columbus, Ohio 43235

DOI: 10.2514/1.46105

A turbine cascade flow control scheme was implemented to simultaneously mitigate secondary flowfield losses using leading-edge endwall suction and spanwise profile losses using vortex generator jet blowing. A proof-of-concept study was performed with a faired cylinder protruding normal from a flat plate. The application of endwall leading-edge suction eliminated the horseshoe-vortex system from the symmetry plane and reduced the total pressure losses by ∼20%. A similar control scheme was then implemented in a turbine cascade. The high-lift turbine blades were equipped with discrete vortex generator jets to maximize loading while maintaining a separation-free flow. At $Re_{Cx} = 25,000$, the wake total pressure losses were dominated by the profile losses (no vortex generator jets). Total pressure data showed that endwall suction eliminated the horseshoe-vortex system but had minimal impact on the wake total pressure losses at both $Re_{Cx} = 25,000$ and 50,000. Simultaneous application of vortex generator jets and leading-edge suction, with matching mass flow rates, reduced the wake losses by 68% at low Re_{Cx}. The horseshoe-vortex system was shown to play a secondary role to the passage vortex in total-pressure-loss generation near the endwall.

Nomenclature

B	=	vortex generator jet blowing ratio
C_x	=	axial chord (0.143 m)
d	=	cylinder diameter (76.2 mm)
H	=	shape factor
$\dot{m}_s$	=	suction slot mass flow rate
P	=	pressure
Re_{Cx}	=	turbine Reynolds number, $\rho U_\infty C_x/\mu$
Re_d	=	cylinder Reynolds number, $\rho U_\infty d/\mu$
r	=	cylinder radial coordinate
SR	=	suction rate (cylinder), $\dot{m}_s/(\rho U_\infty d(\delta_{99} - \delta^*)) \times 100\%$
SR	=	suction rate (turbine), $\dot{m}_s/(\rho U_\infty T(\delta_{99} - \delta^*)) \times 100\%$
T	=	maximum airfoil thickness
U_∞	=	inlet velocity
u	=	streamwise velocity
x	=	cylinder streamwise direction
z	=	cylinder spanwise coordinate
Γ	=	net circulation, $\Delta^2 \Sigma_{i,j} \omega_\theta$
Δ^2	=	differential area of particle image velocimetry grid
δ_{99}	=	boundary-layer thickness
δ^*	=	displacement thickness
θ	=	cylinder angular coordinate
μ	=	dynamic viscosity of air
ρ	=	density of air
ω_θ	=	vorticity in the r-z plane

Subscripts

i, j	=	direction indices
t	=	total
∞	=	inlet conditions

Presented as Paper 2008-4319 at the 4th AIAA Flow Control Conference, Seattle, WA, 23–26 June 2008; received 23 June 2009; revision received 16 March 2010; accepted for publication 23 March 2010.

*Research Associate, Aerospace Engineering; bloxham.2@osu.edu. Student Member AIAA.

†Professor, Aerospace Engineering; bons.2@osu.edu. Associate Fellow AIAA.

I. Introduction

ACCORDING to Sharma and Butler [1], 30–50% of the aerodynamic losses in an axial turbine stator row are attributed to secondary flows in the endwall region. Secondary flows are dominated by a system of interacting vortical structures; the most significant of which are the horseshoe vortex (HV) and passage vortex (PV). The HV (also referred to as the wing-body junction vortex or necklace vortex) occurs in the endwall region as the boundary layer impinges on a bluff body in the flow. The boundary layer is characterized by low-momentum fluid that is retarded by the adverse pressure gradient, due to the downstream presence of the turbine blade leading edge. As a result of the pressure gradient, the boundary layer separates and rolls up into the HV system. A useful schematic of the HV system was provided by Sabatino and Smith [2] (Fig. 1, top). The HV system is composed of at least four vortical structures; the most prominent member of this vortex system is the HV. After the HV forms at the stagnation point, it wraps around the leading edge of the turbine blade. The portions of the vortex that wrap around the suction and pressure surfaces are referred to as the suction side (SSHV) and pressure side legs, respectively. The pressure side of the HV migrates into the turbine passage and merges with the PV. The PV develops due to the intrinsic vortical motion of the boundary layer and the pressure gradients that arise as the flow turns through a curved passage. As the boundary layer moves through the passage the boundary-layer vorticity is reoriented in the streamwise direction. The PV is further strengthened through the passage as the velocity gradients stretch the vortex tube. The structure migrates toward the suction surface endwall region. Its presence creates a three-dimensional boundary-layer separation reducing the turbine blade's ability to produce lift in that region. The trailing-edge endwall separation can cover a significant amount of the total blade span for short aspect ratio blades, as shown by Sharma and Butler [1], Langston et al. [3], and more recently by Palafox et al. [4].

The interaction of the horseshoe and passage vortices has been a topic of debate for the last 60 years. Although the debate has not been entirely resolved, the general consensus is that, to some degree, the flowfield is represented by the secondary flow model provided by Langston [5] (Fig. 1, bottom). Sharma and Butler [1], Goldstein and Spores [6], and Wang et al. [7] have also contributed similar models to the scientific community. The main difference between these models is the treatment of the interaction of the counter-rotating suction-side leg of the HV and the PV. Langston's [5] model suggests that the suction-side leg of the HV remains in the corner region below the PV. Sharma and Butler's [1] model suggests that the suction leg

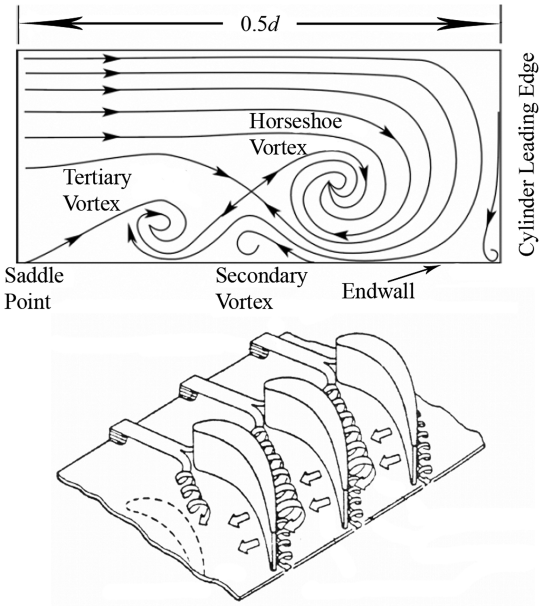

Fig. 1 Representations of the horseshoe-vortex system provided by Sabatino and Smith [2] (top) and the passage vortex system by Langston et al. [3] (bottom).

moves under the PV initially but then wraps multiple times around the PV by the exit of the passage. The model provided by Goldstein and Spores suggests that the suction leg migrates up the span of the suction surface and remains above the PV. A more recent flow visualization study performed by Wang et al. [7] suggests that the suction leg migrates up the span above the PV initially but then wraps once around the PV by the exit of the passage. The existence of so many models attests to the complexity of the flowfield and the difficulty of measuring the flow structures.

Many researchers have attempted to mitigate the total losses due to these structures by altering the development of the HV or PV with varying success. A majority of these studies have used passive control devices including leading-edge modifications (fillets, bulbs, etc.) [8–13], midpitch endwall fences [14,15], and endwall profiling [16,17]. Each of these techniques, when implemented properly, reduced the size and impact of the secondary flows. Active flow control schemes have become increasingly more prevalent in the last ten years. Flow injection [18–20] and removal [21–26] schemes have been attempted. Active flow control has significant promise because the system could be optimized to operate efficiently over a larger flight envelope.

Although the primary focus of this study is secondary flow mitigation in turbomachinery, attempts have been made to reduce the impact of the HV system in external flow applications as well. For example, attempts have been made to minimize the HV system formed at wing-body junctions. The effort has included the use of fillets and leading-edge fairings [12,13], techniques similar to those discussed earlier for turbomachinery flows. Of particular interest to the present study are the flow removal schemes [21,24–26].

Philips et al. [21] used boundary-layer removal at a wing-body junction to reduce the impact of the horseshoe-vortex system. They used a rectangular hole (150 by 190 mm) located on the tunnel wall upstream of the leading edge of a wing model (maximum airfoil thickness T of 140 mm). Five different nondimensional volumetric suction rates were applied. Suction rate was defined as the volume of the boundary layer that was removed relative to the volume flow rate of an undisturbed boundary layer (without the airfoil). A five-hole total pressure probe was used to map the total pressure losses 215 mm downstream of the leading edge adjacent to the airfoil. The results were used to calculate the strength of the horseshoe vortex. The effectiveness of boundary-layer suction was then quantified by calculating net circulation in the region of the vortex. The study showed that net circulation decreased with increasing suction rates and that a nondimensional volumetric flow rate of ~190% was required to effectively eliminate the HV. Unfortunately, the edges of their finite width suction slot acted as streamwise vorticity generators. Consequently, they were unable to fully eliminate the net circulation in the data plane.

Profile losses in the turbine environment also contribute significantly to the total loss. These losses increase dramatically with the onset of boundary-layer separation. As Reynolds number decreases, near-wall momentum in the boundary layer is unable to overcome the adverse pressure gradient, due to the aggressive turning typical of the turbine blade geometry. The result is a significant decrease in lift from the turbine. Both passive and active control techniques have proven effective at decreasing profile losses. Of these separation control techniques, vortex generator jets (VGJs) have shown significant promise [27–29]. One arrangement consists of a spanwise row of VGJs near the peak Cp of the turbine airfoil. The VGJs are used to create streamwise vortical structures and induce boundary-layer transition. Both mechanisms pull high-momentum freestream fluid into the near-wall region reducing the propensity of the flow to separate. Steady and unsteady blowing schemes have both proven effective [27–29].

One of the major concerns with VGJ control schemes is the source of the jet air. Fluid from the compressor could supply the VGJs but at a cost to the work output of the cycle. Ideally, it would be more beneficial to allow this high-energy fluid to move through the combustor and turbine. The previous discussion on flow control of endwall flows suggested that boundary-layer removal could be used to mitigate the secondary losses. The removed fluid becomes a prospective source for the VGJs. A combined flow control scheme could potentially mitigate the losses of both the endwall and midspan without adversely affecting the engine work output. This approach is novel because it focuses on the global losses in the system rather than a single loss source.

This manuscript presents ground-breaking work into the design of an endwall/midspan flow control scheme for a turbine passage. High-loss endwall boundary-layer fluid is removed upstream of the leading edge of a turbine cascade. A comparable amount of fluid is ejected from a midspan row of VGJs. The impact of this global approach to flow control is discussed. As a precursor to the turbine study, an endwall suction flow control scheme was implemented on a faired cylinder protruding from a flat plate. This study was performed to provide insight into the design of the endwall turbine control scheme.

II. Experimental Facilities

A. Cylinder Test Section

The open-loop wind tunnel is powered by a centrifugal blower. After passing through a series of flow conditioners, the air enters a square (0.15 m^2) acrylic duct. At this point, the flow has a $Re_d = 7.5 \times 10^3$ based on the cylinder diameter ($d = 76.2$ mm) and inlet velocity, U_∞. The inlet flow was shown to have a velocity uniformity of $\pm 2\%$, and a freestream turbulence level of less than 1%. An acrylic test section (Fig. 2) is fastened to the end of the wind tunnel duct. The test section height is smaller than the acrylic duct leaving a 20 mm gap at the base of the interface. This gap was added to bleed off the boundary layer that develops in the acrylic duct. The base plate of the test section has a sharp leading edge and is outfitted with a boundary-layer trip. The undisturbed (without the cylinder) boundary-layer

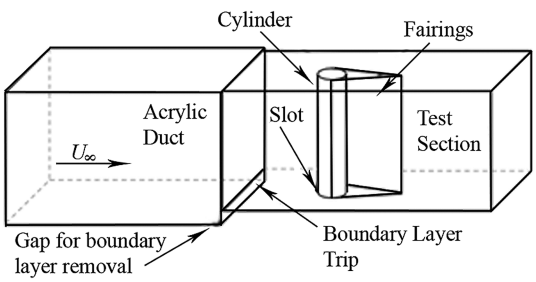

Fig. 2 Schematic of the duct and cylinder test section. Flow moves from left to right.

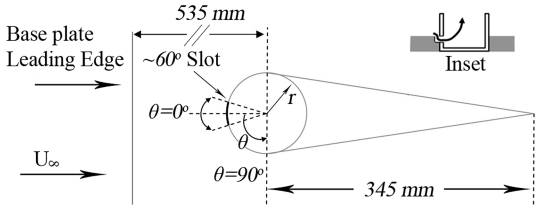

Fig. 3 Top-view schematic of the faired cylinder and coordinate system (+z out of page). The inset depicts the suction slot position relative to the base plate trough.

parameters at the cylinder leading edge were measured using a pitot tube ($\delta_{99} = 41$ mm and $H = 1.54$). These parameters were shown to be uniform across the duct.

A hollow cylinder is mounted to the base plate of the test section duct. Its leading edge is located approximately 0.5 m from the leading edge of the base plate. The cylinder has a 1 mm wide slot near the base of the leading edge (base plate/cylinder interface). The slot extends to approximately $\theta = \pm 30°$ as shown in Fig. 3. The slot is recessed in a trough that was removed from the base plate (inset of Fig. 3). Suction is applied through the slot with a vacuum pump connected to the top of the hollow cylinder. The mass flow removal rate is controlled with a rotameter and a series of valves. Fairings are attached to the sides of the cylinder to eliminate vortex shedding.

B. Cascade Test Section

The three passage linear cascade is composed of four *L1A* turbine blades (Fig. 4). The *L1A* has an axial chord of 0.143 m, a span of 0.38 m, and a solidity of 0.99. Designed by Clark for use in flow control studies [30], the aft loaded *L1A* exhibits massive separation just downstream of the minimum pressure location near 57% C_x for Re_{Cx} below ~50, 000. The two fully immersed blades (labeled inner and outer) house spanwise rows of VGJs near 59% C_x. The VGJs have a diameter of 2.6 mm and are spaced 10d apart. The VGJs have pitch angles of 30° and skew angles of 90°. Pressurized air is fed to the VGJs from a compressor. A pressure regulator is used to regulate the VGJ blowing ratio of $B = 2$, where blowing ratio is defined as the ratio of the jet exit velocity to the local freestream velocity.

A splitter plate is placed 20 mm above the base plate of the test section. The plate is used to condition the boundary layer that impinges on the turbine endwall and also houses the suction slots. The splitter plate has an elliptical leading edge to minimize flow separation. Fluid is also removed below the splitter plate to ensure uniform inlet flow. The splitter plate extends 290 mm upstream of the leading edge of the turbine blades. A 3.2 mm boundary-layer trip is placed near the leading edge of the splitter plate to ensure the development of a turbulent boundary layer. The midpitch boundary-layer parameters were measured in the leading-edge plane with a boundary-layer pitot tube ($\delta_{99} = 20$ mm, $\delta^* = 3.4$ mm, and $H = 1.44$ for $Re_{Cx} = 25000$ and $\delta_{99} = 17$ mm, $\delta^* = 2.7$ mm, and $H = 1.45$ for $Re_{Cx} = 50000$). A 10 mm radius fillet was created at the splitter plate/turbine junction to make the passage geometry more

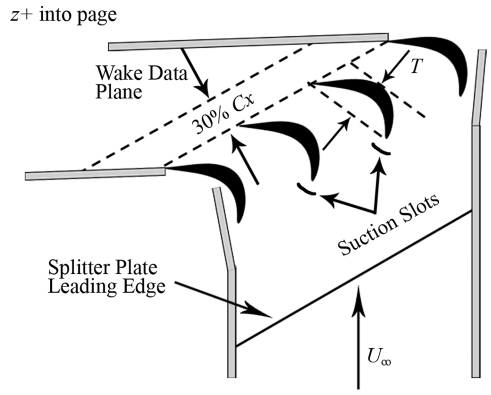

Fig. 4 Schematic of the *L1A* cascade.

representative of an actual engine. Leading-edge suction slots were cut into the splitter plate 12 mm (to slot center) upstream of the turbine leading edge. The slots were connected to a vacuum system with variable suction rates. The suction slot geometry was selected based on the results of the cylinder study and oil-flow visualization studies discussed later. The slots have a nominal width of ~4 mm and length of ~35 mm. They also contain screens to ensure uniform suction across the slots.

C. Suction Rate

The suction rate was varied using a rotameter and a vacuum pump for both the turbine and cylinder configurations. For the cylinder configuration, suction rate [Eq. (1)] is the percentage of the undisturbed (without the cylinder) boundary-layer fluid that is removed through the suction slot. Since the turbine blades could not be removed for an undisturbed boundary-layer measurement, the boundary layer was measured midpitch in the inlet plane. The characteristic length is taken to be the maximum thickness of the turbine ($T = 65$ mm), rather than the diameter. Similar to studies by Sabatino and Smith [2], maximum thickness T (see Fig. 4) was defined as the maximum distance between a normal to the true chord and the suction surface. Maximum airfoil thickness was chosen because it was deemed a more appropriate representation of the width of the fluid area that interacts with the turbine (rather than the leading-edge diameter cylinder). The uncertainty in suction rate was calculated to be ±1%:

$$\mathrm{SR} = \frac{\dot{m}_s}{(\rho U_\infty d(\delta_{99} - \delta^*))} \times 100\% \tag{1}$$

D. Flow Visualization

Flow visualization was performed on the endwall flowfield of the cylinder using a smoke wire and a Nd:YAG laser. The wire (~0.25 mm) was placed 50 mm upstream of the cylinder and oriented perpendicular to the direction of the flow. The laser beam was passed through a cylindrical lens to create a laser sheet in the θ-r plane 10 mm above the base plate. The laser sheet was used to illuminate the smoke particulate caused by the burning of the oil. Visualization of the particulate gave a qualitative glimpse of the horseshoe-vortex formation and migration. It also provided insight into the effectiveness of boundary-layer removal at the base of the airfoil.

Oil-flow visualization (blue printer toner mixed with low-viscosity oil) was also performed on the endwall of the turbine passage. White contact paper was placed on the turbine splitter plate. A thin film of the oil mixture was sprayed onto the contact paper with an atomizer. The splitter plate was then placed in the test section and the wind tunnel was turned on. The resultant flowfield was captured with a standard digital camera. This technique is useful because the velocity gradients remove the toner from regions of higher shear. Streaks in the toner effectively indicate flow direction.

E. Data Acquisition

Total-pressure-loss surveys were measured in the cylinder and the turbine wind tunnels with and without flow control using a Kiel probe. An upstream pitot probe was used as the total pressure reference. The pressure differential was measured using a 0.1 in. H_2O pressure differential transducer. The Kiel probe was mounted to a two-axis traverse above the test sections. For the cylinder, the traverse was used to collect a grid of total pressure measurements in the r-z plane (2 mm increments in r and z) on the 90° plane ($x/d = 0.5$). The grid extended 0.8d in r and 0.53d in z. For the turbine cascade wake and inlet surveys, the traverse collected a coarser grid with a spacing of 5 mm increments in the pitch and span directions. Pressure data were collected across the entire pitch (143 mm) and almost half the total span (~150 mm). Because of the geometry of the Kiel probe, the nearest endwall data points were ~1.8 mm off the surface. The total pressure data were used to gauge the effectiveness of boundary-layer removal and to identify effective

suction rates for each of the test sections. The effectiveness was estimated by calculating a normalized area-average total pressure difference $(P_{t_\infty} - P_t)/(P_{t_\infty} - P_{s_\infty})$. The uncertainty in the area-average total pressure losses was calculated to be $\pm 4\%$.

Data were also collected on the cylinder test section using a LaVision particle image velocimetry (PIV) system. The Nd:YAG laser was positioned below the test section. Two consecutive laser sheets (1 mm thick) were projected into the test region with a time separation of 200 μs. This time separation allowed for in-plane motion without allowing the particle seed to pass through the laser sheet. The flow was seeded with 1–2 μm olive oil particles. The high-speed camera had a resolution of 1376×1040 pixels and captured a total viewing window of approximately 70 mm $\times$ 50 mm. Date were collected on the symmetry plane and the 90° plane with and without leading-edge boundary-layer removal. At each location 300 images were captured and averaged together using the LaVision software [31]. Vector processing was initially performed with 64×64 pixels interrogation windows. The interrogation windows were then refined to 16×16 pixels. A 50% overlap was used during the vector processing.

According to LaVision the uncertainty in the seed particle displacement was approximately 0.2 pixels. Coupled with a 95% confidence interval estimate of the uncertainty in the freestream velocity, the total uncertainty in velocity is 5%. After calculating the velocity vectors, these data were used to calculate the vorticity with a central difference approximation. A top-hat filter was applied to the resultant vorticity field to eliminate erroneous large scale fluctuations of vorticity. A bandpass filter was also applied to the vorticity field to eliminate small fluctuations about zero. Net circulation was calculated with the vorticity data using Eq. (2) provided by Philips et al. [21], where Δ^2 is the smallest differential area of the PIV grid. The uncertainty in circulation was calculated to be 7%:

$$\Gamma = \Delta^2 \sum_{i,j} \omega_\theta \tag{2}$$

III. Results

A. Cylinder Configuration

1. Smoke–Wire Visualization: Cylinder

Smoke–wire visualization was used to obtain a qualitative assessment of the effectiveness of boundary-layer removal on the HV formation for the cylinder test section. A standard video camera was used to take footage of the HV with and without suction. Figure 5 contains two still images from the video. The left and right images were taken while the suction was turned off and on, respectively. It should be noted that the boundary-layer flow in these images is laminar and the Re_d is 3750 (50% lower than the nominal value). The Re_d was decreased and the boundary-layer trip was removed to facilitate the visualization of the HV system. The remainder of the data presented in this work was obtained with the boundary-layer trip.

A comparison of the images in Fig. 5 shows that removing a portion of the impinging boundary layer at the cylinder base significantly alters the near-wall flowfield. The image without suction clearly depicts a horseshoe vortex that wraps completely around the bluff body. As the boundary layer and smoke propagate toward the cylinder the adverse pressure gradient causes boundary-layer separation. Once the near-wall fluid separates the higher momentum fluid rolls over the stagnant air. The tertiary vortex is also visible upstream of the HV. When suction is applied the smoke traces do not suggest the formation of an HV. Instead, the smoke traces move directly to the suction slot or around the cylinder.

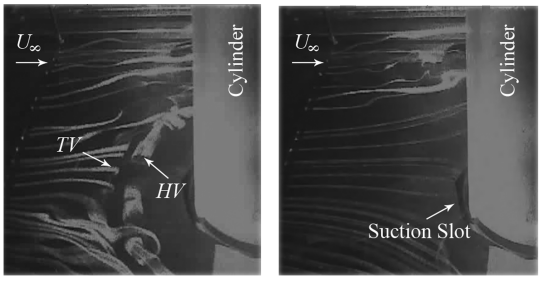

a) No Suction **b) Suction (11.0%)**

Fig. 5 Smoke—wire visualization depicting the impact of boundary-layer removal on the horseshoe vortex; $Re_d = 3750$.

2. Total Pressure Losses: Cylinder

The area-average total pressure losses on the cylinder were calculated for each suction rate and then normalized by the area-average total pressure losses without suction. Figure 6 contains the normalized integrated total pressure losses obtained for each of the suction rates measured at $0.5d$ (90° plane) and $2.5d$ downstream of the leading edge of the cylinder. A value of 1 on the ordinate axis indicates that there was no effect of the suction rate on the integrated total pressure losses. The trend of both data sets appears to be an asymptotic decrease in the total pressure losses with increasing suction rates. The uncertainty bars ($\pm 4\%$) are included to illustrate that the losses at a suction rate of 11% may not represent an optimum. Regardless, the trend of both data sets ($0.5d$ and $2.5d$) suggests that there may be an inflection in the loss curves between 11 and 20%.

3. Particle Image Velocimetry: Cylinder

Figure 7 contains contour plots of the time-mean symmetry plane vorticity taken from the PIV data with and without leading-edge boundary-layer removal (SR = 11%). The vorticity is normalized by the ratio of the freestream velocity and the diameter of the cylinder. The black region near $r/d = 0.5$ is a shadow caused by the obstruction of the base plate suction slot on the laser sheet. The leading edge of the cylinder and the base plate are located at $r/d = 0.5$ and $z/d = 0$, respectively. Streamline topologies were added to further define the flow structures.

The HV is visible in the no suction plot between $r/d = 0.6$ and 0.8 as a region of elevated negative vorticity. The vortex resides in two different regions, as illustrated by the elevated vorticity near $r/d = 0.75$ (primary position) and $r/d = 0.63$ (secondary position). This bimodal behavior has been observed in the symmetry plane by various groups [2,26,32,33]. The position of the primary time-mean HV is about $0.24r/d$ from the cylinder wall and $0.06z/d$ from the base plate. The vertical position is similar to that observed by Praisner and Smith [32], but the streamwise position is closer to the cylinder in their data ($0.18r/d$).

The streamline topologies clearly capture the primary position of the HV. The location of the tertiary vortex (TV) is also visible in the streamlines (though not as clear). Its farthest downstream extent is near $r/d = 0.85$. At this point the streamlines change direction, delineating the vortex. The secondary vortex (SV) is evident between the HV and TV as a region of positive vorticity in the near-wall region near $r/d = 0.77$. Its location is further evidenced by the bending of

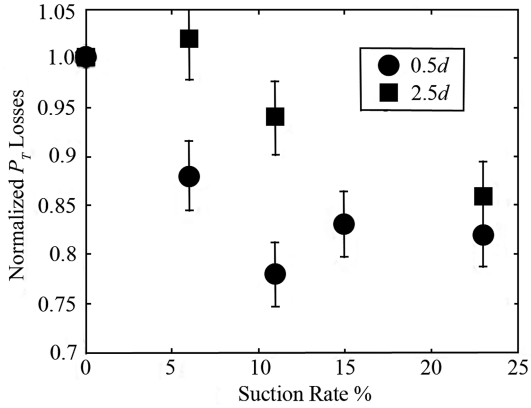

Fig. 6 The impact of suction rate on the area-average total pressure losses on the cylinder, $(P_{t_\infty} - P_t)/(P_{t_\infty} - P_t)_{SR=0}$.

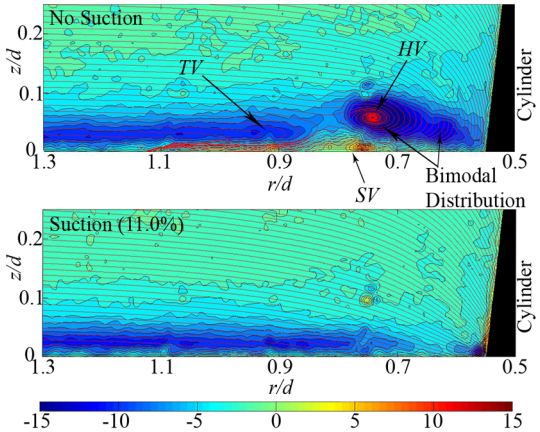

Fig. 7 Normalized time-mean symmetry plane vorticity, $\omega_\theta/(U_\infty/d)$, and streamline topologies on the cylinder. The black region is a shadow caused by the suction slot.

the streamlines away from the HV near $r/d = 0.80$. The band of negative vorticity that extends from $r/d = 0.9$ to $r/d = 1.3$ is the vorticity created by the velocity gradients in the boundary layer.

Applying boundary-layer suction (SR = 11%) significantly alters the time-mean symmetry plane vorticity field. The primary difference is the negative vorticity associated with the HV is no longer present in the flowfield. Consequently, the *SV* and TV are also no longer present. The streamline topologies demonstrate flow migration down to the suction slot. This flow migration suggests that the adverse pressure gradient has been removed. The band of negative vorticity embedded in the boundary layer is still present and extends all the way to $r/d = 0.7$.

In a turbine passage, the pressure-side leg of the HV migrates toward the suction surface of the adjacent turbine blade. As it crosses the passage it interacts with the PV resulting in the complex flowfield described earlier (Fig. 1). In the faired cylinder configuration, there are no adjacent blades or curved passages to strengthen the vortex. Regardless, the downstream impact of boundary-layer removal is still of interest to validate the effectiveness of leading-edge suction. Figure 8 contains time-mean normalized vorticity plots at the 90° plane with and without leading-edge suction. The no suction plot still clearly shows the presence of the HV. The strength of the vortex has decreased (by ∼50%) but the bimodal shape is still evident. The position of the vortex in the 90° plane is similar to the results of Praisner and Smith [34]. Also of interest in the no suction vorticity contour of Fig. 8 is the positive corner vortex seen near $r/d = 0.55$. This region of positive vorticity, spanning the right side of the plot from $z/d = 0$ to $z/d > 0.25$, is also consistent with the results of Praisner and Smith. The authors believe that this band of vorticity is generated by the horseshoe vortex as it sweeps fluid down the cylinder to the endwall. As the flow moves down along the cylinder leading edge, boundary layers form. The boundary-layer-generated vorticity then travels around the leading edge and presents itself along the span in Fig. 8 as a band of positive vorticity. In light of this discussion, the spanwise vorticity should decrease in magnitude away from the endwall. The maximum vorticity value of 15 is near $z/d = 0.1$. Above the maximum value, the vorticity monotonically decreases as span increases. As evidence that this positive vorticity band is related to the horseshoe-vortex system, as suction reduces the HV, the positive vorticity decreases as well (Fig. 8).

The corresponding normalized vorticity plot with suction (11.0%) does not exhibit a concentrated negative vortex structure, although the negative vorticity band is still present. It extends from near the cylinder wall to $r/d = 1.3$. By this point, the vorticity has almost completely dissipated. Vorticity in the corner vortex region has decreased by ∼33%. The maximum vorticity in the corner vortex with suction is found at the same spanwise location as the no suction data.

PIV data were also taken $1.5d$ downstream of the leading edge of the faired cylinder. These data were used to calculate the net nondimensional circulation ($\Gamma/d \cdot U_\infty$) for each of the suction rates used in this study. The results are compared with the results of Philips et al. [21] in Fig. 9. The present study fills a void in the data of Philips et al. The data depict a more rapid decrease in the net nondimensional circulation for lower suction rates. Unlike the total pressure losses presented in Fig. 6, the circulation decreases monotonically with increasing suction up to suction rates of 200%. This result bodes well for applications of secondary flow control using suction.

The cylinder study provided insight into the design of a similar control scheme for the turbine environment. The main conclusion from the cylinder study is that applying leading-edge suction can effectively eliminate the formation of the HV system. Suction alters the adverse pressure gradient that causes the vortex to form. Instead, a favorable pressure gradient develops that accelerates the near-wall fluid. An inflection in the total-pressure-loss data shows a minimal increase in pressure loss reduction for suction rates greater than 11%. Thus, suction rate can be optimized to have maximum benefit while minimizing fluid extraction. As stated earlier, Sabatino and Smith [2] suggested that Reynolds number scaling of horseshoe-vortex systems on cylinders and airfoils should be based on the cylinder diameter and the maximum thickness of the turbine blade as the characteristic lengths, respectively. Accordingly, a similar scaling arrangement was used in the present study to set both Reynolds number near 10 K.

B. Turbine Configuration

1. *Oil-Flow Visualization: Turbine Passage*

Oil-flow visualization was used to obtain a qualitative assessment of the turbine endwall flow before the suction slots were added. Figure 10 contains an image of the center passage of the turbine endwall at $Re_{Cx} = 50,000$. The black turbine blades protrude from

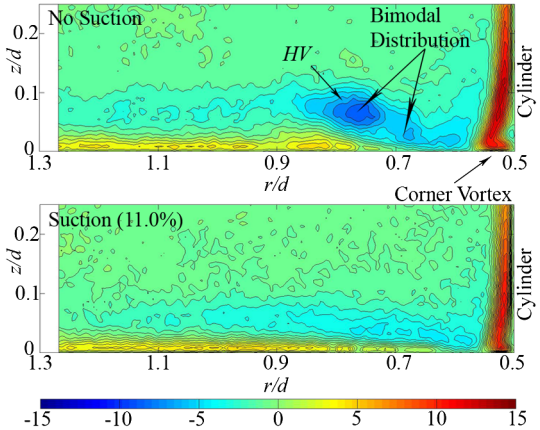

Fig. 8 Time-mean normalized vorticity, $\omega_\theta/(U_\infty/d)$, on the 90° plane of the cylinder.

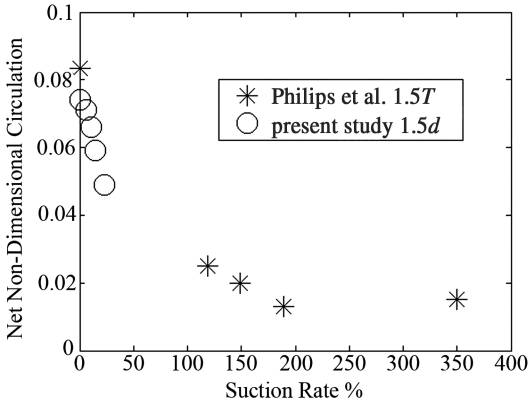

Fig. 9 Net nondimensional circulation ($\Gamma/d \cdot U_\infty$) from the present study and Philips et al. [21].

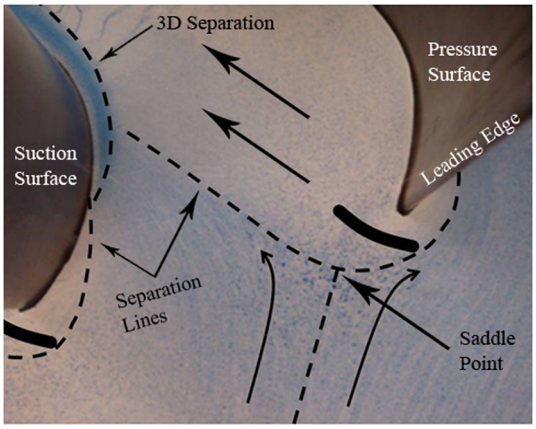

Fig. 10 Oil-flow visualization of the inlet endwall of the turbine passage. The dashed lines represent critical lines. $Re_{Cx} = 50000$.

the white contact paper-covered splitter plate. The leading edge and suction surface of the inner turbine blade are visible on the left side of the image. The outer turbine blade leading edge and pressure surface are clearly visible on the right. The dashed lines represent critical lines in the flowfield. They were positioned with the aid of the streaks left behind by the ink toner. The streaks show the trajectory of the main flow features in the endwall including the passage vortex, the 3-D separation region, and the suction and pressure-side legs of the horseshoe vortex. The saddle point of the outer turbine blade is located upstream and slightly to the left of the turbine leading edge. This topological feature is the genesis of the passage and horseshoe vortices and a juncture of flow separation. The flow on the right side of the dividing streamline rolls into the suction side of the outer blade horseshoe vortex. The flow on the left side of the dividing streamline forms the passage vortex. The cross passage migration of the PV and the suction surface three-dimensional separation are also visible. It is interesting to note that the upstream inception of the three-dimensional separation occurs where the suction-side HV separation line meets the endwall/suction surface juncture instead of where the PV meets the suction surface. This was seen previously by Gbadebo et al. [35] in their study on compressor endwall flow topology. The three-dimensional separation is characterized by lower shear stresses. Consequently, the ink toner accumulates in this region.

These topological features and the results of the cylinder study were used to position the suction slots (the black arcs directly in front of the turbine leading edges in Fig. 10). The slots were positioned midway between the saddle point and the turbine blade leading edges. Ideally, the suction slots would have been placed directly upstream of the leading edges to reduce the impact of incidence angle on the flow control scheme. Unfortunately, this was not possible, due

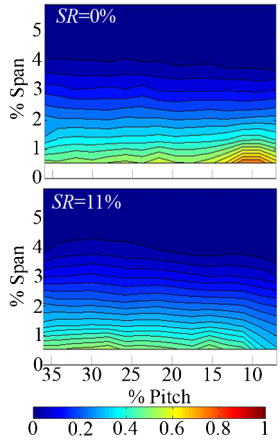

Fig. 11 Inlet plane total-pressure-loss surveys with (bottom) and without (top) leading-edge suction. The inner and outer blade leading edges represent 0 and 100% pitch, respectively; $(P_{t_\infty} - P_t)/(P_{t_\infty} - P_{s_\infty})$.

to the endwall/turbine fillets. The fillets were not included in the oil-flow visualization study, but in the final configuration the 10-mm-radius fillets extend to the suction slots. The slots also extend into the turbine passages on both sides of the turbine blades with the intent of eliminating the adverse pressure gradient that drives the formation of the horseshoe-vortex structures.

2. *Inlet Total Pressure Surveys: Turbine*

Total pressure surveys in the inlet plane endwall region of the turbine passage illustrate the impact of suction on the horseshoe vortex. Figure 11 contains normalized total pressure data without leading-edge suction (top) and with 11% leading-edge suction (bottom) at $Re_{Cx} = 25,000$. The contour plots are presented from a downstream (looking upstream) frame of reference. The leading edges of the inner and outer turbine blades are 0 and 100% pitch, respectively. Because of geometry limitations the nearest wall proximity to the inner turbine blade leading edge was ~6% pitch. Data are not presented across the full extent of the inlet plane given that the HV only resides in small localized areas. The focus of the data window presented in Fig. 11 is the SSHV. The impact of the SSHV is clearly evident in the no suction total pressure data near 10% pitch. The SSHV collects high-loss fluid from the boundary layer, which results in elevated total pressure loss. When suction is applied at 11% the total-pressure-loss core is eliminated from the inlet plane. It can also be inferred that the SSHV is likewise eliminated. Similar qualitative results were also measured at $Re_{Cx} = 50,000$ and SR = 11%.

3. *Wake Total Pressure Surveys: Turbine*

Total-pressure-loss wake surveys were also collected 30% C_x downstream of the turbine blades at $Re_{Cx} = 25,000$ and 50,000. These data were used to gauge the impact of suction and VGJ actuation on the total pressure losses in the turbine cascade environment. At $Re_{Cx} = 25,000$, the suction surface of the turbine exhibits a massive separation. Figure 12 contains contour plots of the normalized total pressure losses with (right) and without (left) VGJ actuation and no endwall suction (SR = 0). The contour plots are presented from a downstream (looking upstream) frame of reference. The no VGJ plot shows significant total pressure loss, particularly in the spanwise separation region. The total pressure losses are highest near midspan (loss near 4) and decrease in the near-wall region where the PV resides. The presence of the PV reduces the spanwise extent of the 2-D blade separation as a result of momentum transfer due to the rotation of the vortex. When the VGJs are activated ($B = 2$), there is a significant change in the downstream total pressure losses (68% decrease) and the wake trajectory. With VGJs, the 2-D blade separation is eliminated or greatly reduced. The wake trajectory shifts toward the right side of the data window. The loss core of the PV also changes magnitude and position. The loss core shifts to the right ~10% pitch and away from the endwall ~5% span. One might suppose that the addition of midspan VGJ actuation would negatively impact the endwall flowfield. The present results show that, in fact, this particular VGJ configuration positively impacts the endwall flowfield, as seen by a 25% reduction in the magnitude of the loss core (from ~2 to ~1.5).

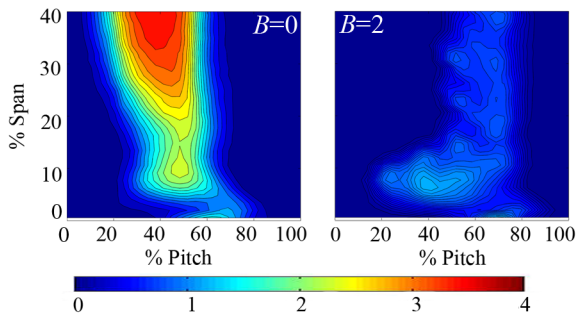

Fig. 12 Total-pressure-loss wake surveys with (right) and without (left) VGJ actuation. $Re_{Cx} = 25,000$, SR = 0, and $(P_{t_\infty} - P_t)/(P_{t_\infty} - P_{s_\infty})$.

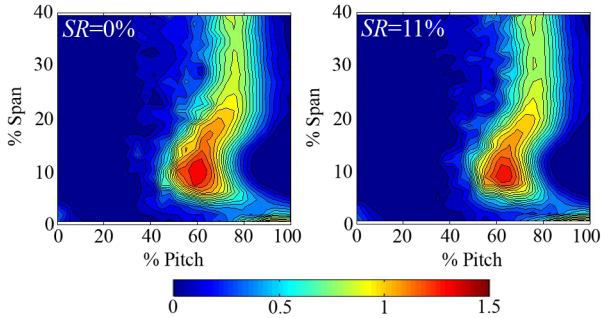

Fig. 13 Total-pressure-loss wake surveys with (right) and without (left) leading-edge suction. $Re_{Cx} = 50,000$, $B_{\max} = 0$, and $(P_{t_\infty} - P_t)/(P_{t_\infty} - P_{s_\infty})$.

The undulations evident in the midspan wake of Fig. 12 (right) are caused by the steady VGJs. As mentioned earlier, steady VGJs promote mixing by the creation of streamwise vorticity and boundary-layer transition. The vortical structures pull high-momentum fluid into the near-wall region while dragging low-momentum fluid into the freestream. The result is a broad wake with pockets of higher-loss fluid downstream of the VGJ injection sites. These structures contribute to the overall loss measurement. As could be expected, the losses associated with streamwise vorticity increase as the blowing ratio increases for an attached flow. Thus, the designer could minimize the profile losses by employing lower blowing ratios while still maintaining a separation-free flowfield. At higher Re_{Cx}, the VGJs are not needed for boundary-layer reattachment on the *L1A*. Consequently, they have a detrimental impact on the total pressure losses.

When leading-edge endwall suction at SR = 11% was included with VGJs, there was minimal additional reduction to the total pressure losses. At these settings ($B = 2$ and SR = 11%) the mass flow ratio between the VGJs and the suction slots was 1:1. It should be noted that while the mass flows were matched, the two systems were actuated separately. Although the removed fluid is not injected through the VGJs, the results do demonstrate the potential of a combined zero-net mass flux flow control system.

Given the small impact of suction at 11%, data were also collected at suction rates approaching 20%. Similar to the results of the cylinder study, suction rates above 11% had minimal additional impact on total-pressure-loss reduction. Given the significance of the 2-D profile losses compared with the endwall losses, the secondary loss reduction due to leading-edge suction was difficult to gauge. An attempt was made to isolate the impact of suction on the total pressure losses by increasing the Re_{Cx} of the flow to 50,000. At this Re_{Cx}, the spanwise flowfield does not exhibit boundary-layer separation. Consequently, any change in the wake total pressure losses can be directly attributed to leading-edge flow control.

Figure 13 contains contour plots of normalized total pressure loss in the turbine wake with (right) and without (left) leading-edge suction at SR = 11%. Suction resulted in a 7% decrease in the area-average total pressure losses. Subtle changes in the shape, magnitude, and position of the total-pressure-loss core are also noted. Unlike the cylinder study, leading-edge suction in the turbine cascade did not eliminate the downstream loss core. It was shown in Fig. 11 that the HV was eliminated in the cascade inlet plane with a suction rate of 11%. The continued presence of the majority of the loss structure in the wake (with suction) suggests that the horseshoe vortex is a secondary contributor to the generation of turbine endwall loss. Consequently, the authors suggest that an effective secondary loss reduction scheme should focus on altering the mechanisms that drive the formation of the PV system as well as the HV system.

IV. Conclusions

A flow control scheme was implemented that simultaneously mitigated profile and endwall losses by employing spanwise VGJ blowing and leading-edge suction. The combined system had an approximate zero-net mass flux. At low Re_{Cx}, the profile losses dominated the wake total pressure losses. Application of VGJ blowing resulted in a 68% reduction in the area-averaged total pressure losses in the wake. The addition of leading-edge suction at a suction rate of 11% provided minimal additional reductions. Similar to the cylinder study, suction rates greater than 11% did not provide additional reductions in the total pressure losses in the wake. At higher Re_{Cx}, leading-edge suction at 11% (without VGJs) resulted in a 7% decrease in the total pressure losses in the wake. Inlet plane total-pressure-loss data showed that the horseshoe-vortex structure was eliminated with SR = 11% for both Re_{Cx}. The complete removal of the HV coupled with the slight reductions in wake loss (with SR = 11%) suggests that the horseshoe-vortex system is a secondary contributor to endwall total-pressure-loss generation.

Acknowledgments

The authors thank NASA for sponsorship of this project under NASA grant NNX07AE04A with Anthony Strazisar as Project Monitor. The experimental portion of this study could not have been done without the able assistance of Rebecca Hollis, Jon Pluim, and Kyle Gompertz.

References

[1] Sharma, O., and Butler, T., "Predictions of Endwall Losses and Secondary Flows in Axial Flow Turbine Cascades," *Journal of Turbomachinery*, Vol. 109, 1987, pp. 229–236. doi:10.1115/1.3262089

[2] Sabatino, D. R., and Smith, C. R., "Boundary Layer Influence on the Unsteady Horseshoe Vortex Flow and Surface Heat Transfer," ASME Turbo Expo 2007: Power by Land, Sea, and Air, American Society of Mechanic Engineers, Paper GT2007-27633, 2007.

[3] Langston, L. S., Nice, M. L., and Hooper, R. M., "Three-Dimensional Flow in a Turbine Cascade Passage," *Journal of Engineering for Power*, Vol. 99, 1977, pp. 21–28.

[4] Palafox, P., Oldfield, M. L. G., LaGraff, J. E., and Jones, T. V., "PIV Maps of Tip Leakage and Secondary Flow Fields on a Low-Speed Turbine Blade Cascade with Moving End Wall," *Journal of Turbomachinery*, Vol. 130, 2008, Paper 011001. doi:10.1115/1.2437218

[5] Langston, L. S., "Crossflows in a Turbine Cascade Passage," *Journal of Engineering for Power*, Vol. 102, 1980, pp. 866–874. doi:10.1115/1.3230352

[6] Goldstein, R. J., and Spores, R. A., "Turbulent Transport on the Endwall in the Region Between Adjacent Turbine Blades," *Journal of Heat Transfer*, Vol. 110, 1988, pp. 862–869. doi:10.1115/1.3250586

[7] Wang, H. P., Olson, S. J., Goldstein, R. J., and Eckert, E. R. G., "Flow Visualization in a Linear Turbine Cascade of High Performance Turbine Blades," *Journal of Turbomachinery*, Vol. 119, 1997, pp. 1–8. doi:10.1115/1.2841006

[8] Becz, S., Majewski, M. S., and Langston, L. S., "An Experimental Investigation of Contoured Leading Edges for Secondary Flow Loss Reduction," *ASME Turbo Expo 2004: Power by Land, Sea, and Air*, American Society of Mechanic Engineers, GT2004-53964, 2004.

[9] Sauer, H., Muller, R., and Vogeler, K., "Reduction of Secondary Flow Losses in Turbine Cascades by Leading Edge Modifications at the Endwall," *Journal of Turbomachinery*, Vol. 123, 2001, pp. 207–213. doi:10.1115/1.1354142

[10] Zess, G. A., and Thole, K. A., "Computational Design and Experimental Evaluation of Using a Leading Edge Fillet on a Gas Turbine Vane," *Journal of Turbomachinery*, Vol. 124, 2002, pp. 167–175. doi:10.1115/1.1460914

[11] Muller, R., Sauer, H., and Vogeler, K., "Influencing the Secondary Losses in Compressor Cascades by a Leading Edge Bulb Modification at the Endwall," ASME Turbo Expo 2002: Power by Land, Sea, and Air, American Society of Mechanic Engineers, Paper GT-2002-30442, 2002.

[12] Devenport, W. J., Agarwal, N. K., Dewitz, M. B., Simpson, R. L., and Poddar, K., "Effects of a Fillet on the Flow Past a Wing-Body Junction," *AIAA Journal*, Vol. 28, No. 12, 1990, pp. 2017–2024. doi:10.2514/3.10517

[13] Devenport, W. J., Simpson, R. L., Dewitz, M. B., and Agarwal, N. K., "Effects of a Leading-Edge Fillet on the Flow Past an Appendage-Body Junction," *AIAA Journal*, Vol. 30, No. 9, 1992, pp. 2177–2183. doi:10.2514/3.11201

[14] Chung, J. T., Simon, T. W., and Buddhavarapu, J., "Three-Dimensional Flow near the Blade/Endwall Junction of a Gas Turbine: Application of a Boundary Layer Fence," American Society of Mechanic Engineers, Paper 91-GT-45, 1991.
[15] Chung, J. T., and Simon, T. W., "Effectiveness of the Gas Turbine Endwall Fences in Secondary Flow Control at Elevated Freestream Turbulence Levels," ASME Paper 93-GT-51, 1993.
[16] Harvey, N. W., Rose, M. G., Shahpar, S., Taylor, M. D., Hartland, J., and Gregory-Smith, D. G., "Non-Axisymmetric Turbine End Wall Design: Part I-Three-Dimensional Design System," *Journal of Turbomachinery*, Vol. 122, 2000, pp. 278–285. doi:10.1115/1.555445
[17] Ingram, G., Gregory-Smith, D., Rose, M., Harvey, N., and Brennan, G., "The Effect of End-Wall Profiling on Secondary Flow and Loss Development in a Turbine Cascade," ASME Turbo Expo 2002: Power for Land, Sea, and Air, American Society of Mechanic Engineers, Paper GT-2002-30339, 2002.
[18] Aunapu, N. V., Volino, R. J., Flack, K. A., and Stoddard, R. M., "Secondary Flow Measurements in a Turbine Passage with Endwall Flow Modification," *Journal of Turbomachinery*, Vol. 122, 2000, pp. 651–658. doi:10.1115/1.1311286
[19] Rehder, H. J., and Dannhauer, A., "Experimental Investigation of Turbine Leakage Flows on the Three-Dimensional Flow Field and Endwall Heat Transfer," *Journal of Turbomachinery*, Vol. 129, 2007, pp. 608–618. doi:10.1115/1.2720484
[20] de la Rosa Blanco, E., Hodson, H. P., and Vazquez, R., "Effect of the Leakage Flows and the Upstream Platform Geometry on the Endwall Flows of a Turbine Cascade," ASME Turbo Expo 2006: Power for Land, Sea, and Air, American Society of Mechanic Engineers, GT-2006-90767, 2006.
[21] Philips, D. B., Cimbala, J. M., Treaster, A. L., "Suppression of the Wing-Body Junction Vortex by Body Surface Suction," *Journal of Aircraft*, Vol. 29, No. 1, 1992, pp. 118–122. doi:10.2514/3.46134
[22] Gummer, V., Goller, M., and Swoboda, M., "Numerical Investigation of End Wall Boundary Layer Removal on Highly Loaded Axial Compressor Blade Rows," *Journal of Turbomachinery*, Vol. 130, 2008, Paper 011015. doi:10.1115/1.2749297
[23] Gbadebo, S. A., Cumpsty, N. A., and Hynes, T. P., "Control of Three-Dimensional Separations in Axial Compressors by Tailored Boundary Layer Suction," *Journal of Turbomachinery*, Vol. 130, 2008, Paper 011004. doi:10.1115/1.2749294
[24] Johnson, M., Ravindra, K., and Andres, R., "Comparative Study of the Elimination of the Wing Fuselage Junction Vortex by Boundary Layer Suction and Blowing," 32nd AIAA Aerospace Sciences Meeting and Exhibit, Reno NV, Jan. 1994, AIAA Paper 94-0293, 1994.
[25] Barberis, D., Molton, P., and Malaterre, T., "Control of 3-D Turbulent Boundary Layer Separation Caused by a Wing-Body Junction," *Experimental Thermal and Fluid Science*, Vol. 16, 1998, pp. 54–63. doi:10.1016/S0894-1777(97)10012-7
[26] Seal, C. V., and Smith, C. R., "The Control of Turbulent End-Wall Boundary Layers Using Surface Suction," *Experiments in Fluids*, Vol. 27, 1999, pp. 484–496. doi:10.1007/s003480050373
[27] Volino, R. J., "Separation Control on Low-Pressure Turbine Airfoils Using Synthetic Vortex Generator Jets," *Journal of Turbomachinery*, Vol. 125, 2003, pp. 765–777. doi:10.1115/1.1626686
[28] Sondergaard, R., Rivir, R., and Bons, J., "Control of Low-Pressure Turbine Separation Using Vortex-Generator Jets," *Journal of Propulsion and Power*, Vol. 18, No. 4, 2002, pp. 889–895. doi:10.2514/2.6014
[29] Bons, J. P., Sondergaard, R., and Rivir, R., "Turbine Separation Control Using Pulsed Vortex Generator Jets," *Journal of Turbomachinery*, Vol. 123, 2001, pp. 198–206. doi:10.1115/1.1350410
[30] Bons, J., Pluim, J., Gompertz, K., Bloxham, M., and Clark, J., "The Application of Flow Control to an Aft-Loaded Low Pressure Turbine Cascade with Unsteady Wakes," ASME Turbo Expo 2008: Power for Land, Sea, and Air, June 2008, Berlin, Germany, American Society of Mechanic Engineers, Paper GT2008-50864, 2008.
[31] Davis Flowmaster, Software Package, Ver. 7.0, March 2004, LaVision GmbH, Gottingen, Germany, 2004.
[32] Praisner, T. J., and Smith, C. R., "The Dynamics of the Horseshoe Vortex and Associated Endwall Heat Transfer—Part I: Temporal Behavior," *Journal of Turbomachinery*, Vol. 128, 2006, pp. 747–754. doi:10.1115/1.2185676
[33] Devenport, W. J., and Simpson, R. L., "Time-Dependent and Time-Averaged Turbulence Structure Near the Nose of a Wing-Body Junction," *Journal of Fluid Mechanics*, Vol. 210, 1990, pp. 23–55. doi:10.1017/S0022112090001215
[34] Praisner, T. J., and Smith, C. R., "The Dynamics of the Horseshoe Vortex and Associated Endwall Heat Transfer—Part II: Time-Mean Results," *Journal of Turbomachinery*, Vol. 128, 2006, pp. 755–762. doi:10.1115/1.2185677
[35] Gbadebo, S. A., Cumpsty, N. A., and Hynes, T. P., "Three-Dimensional Separations in Axial Compressors," *Journal of Turbomachinery*, Vol. 127, No. 2, 2005, pp. 331–339. doi:10.1115/1.1811093

F. Liu
Associate Editor